Thermal stability, corrosion resistance and nano-indentation behavior of $Ni_{60}Nb_{40-x}Zr_x$ (X= 0, 20, 40) amorphous alloys

Moein Imani*[,1], Reihane Aliramezani[1], Esmat Dastanpour[1,2], Hamidreza Yousefi-Zavieh[1], Mohammad Hossein Enayati[1]

[1]*Department of Materials Engineering, Isfahan University of Technology, Isfahan, Iran;*
[2]*Department of Materials Science and Engineering, KTH Royal Institute of Technology, Stockholm, Sweden.*

Corresponding author email: moein.imani91@gmail.com

ABSTRACT

In this research, thermal stability, corrosion performance, hardness (H), and Young modulus (E) of $Ni_{60}Nb_{40}$, $Ni_{60}Nb_{20}Zr_{20}$, and $Ni_{60}Zr_{40}$ amorphous ribbons were evaluated during the differential scanning calorimetry (DSC), electrochemical impedance spectroscopy (EIS) and potentiodynamic polarization tests, and nanoindentation technique, respectively. Results showed that the onset crystallization temperatures (T_o) of $Ni_{60}Nb_{40}$, $Ni_{60}Nb_{20}Zr_{20}$, and $Ni_{60}Zr_{40}$ amorphous ribbons were 632 °C, 593 °C and 476 °C, respectively. It is determined that the higher Nb content increases the thermal stability against crystallization. Evaluation of corrosion resistance during potentiodynamic polarization test showed the polarization resistance value of 936 , 49, and 16 $M\Omega.cm^2$ for $Ni_{60}Nb_{40}$, $Ni_{60}Nb_{20}Zr_{20}$, and $Ni_{60}Zr_{40}$ alloys, respectively. These results imply that the substitution of Zr with Nb enhances the thermal stability and corrosion resistance of Ni-Nb-Zr amorphous ribbons. Moreover, the H and E for $Ni_{60}Nb_{40}$, $Ni_{60}Nb_{20}Zr_{20}$, and $Ni_{60}Zr_{40}$ amorphous ribbons were 171.3 and 15.01 GPa, 160.41 and 12.16 GPa, and, 188.52 and 14.13 GPa, respectively. It means complete substitution of Zr by Nb in Ni-Nb-Zr amorphous ribbons shows the highest hardness which is related to the $Ni_{60}Nb_{40}$ amorphous ribbon.

Keywords: Ni-based amorphous alloys, thermal stability, corrosion resistance, nano-indentation.

1. Introduction

Amorphous alloys have several unique characteristics such as good mechanical properties, high corrosion resistance, and enhanced magnetic properties, which lead to a wide variety of applications in different industries [1]. Furthermore, it is possible to produce nanocrystalline structures or nanocrystalline-amorphous composites by controlled crystallization of amorphous structure [1-3]. Among various amorphous alloys, Ni-based amorphous alloys have a combination of properties such as good thermal stability, high mechanical properties, and desirable corrosion resistance that make them suitable for engineering applications such as precision gears, pressure sensors in automobile, hydrogen membrane, separators in fuel cells and so forth [1, 4]. The most studied Ni-based amorphous alloys are Ni-Nb [5-7], Ni-Zr [6, 8], Ni-Mo [9], Ni-Ti and Ni-Hf [10], Ni-P [11, 12], Ni-Nb-Zr [6, 13-20], Ni-Nb-Ta-Zr [21], Ni-Zr-Ti and Ni-Zr-Hf [10]. Among many Ni-based alloy systems, Ni–Nb, Ni-Zr and Ni-Nb-Zr alloy systems are the most widely studied in terms of glass-forming ability (GFA), mechanical properties and hydrogen permeability [6, 8, 16, 22]. Based on binary phase diagrams of Ni-Nb, Ni-Zr, and experiment results, the highest GFA was obtained to be around 60 % at. Ni content. Furthermore, Kimura et al. [16] showed that in the ternary Ni-Nb-Zr system, alloy containing ~ 60 % at. Ni, 20 %

at. Nb, and 20 % at. Zr had the highest GFA. Alloys with their GFA are shown in the ternary Ni-Nb-Zr phase diagram in Fig. 1.

Dolan et al. [23] reported that for binary and ternary Ni–early transition metals (ETM) - eutectic alloys, the addition of ETM elements such as Nb and Zr lead to a dramatic change in properties of Ni-based amorphous alloys. The presence of Zr element in Ni-based amorphous alloys increases the hydrogen permeability but descends the thermal stability [18]. The effect of Zr content on the mechanical properties of Ni-based amorphous alloys is contradictory [21, 24]. On the other side, the addition of Nb to Ni-based amorphous alloys improves some mechanical properties such as Young modulus and hardness, as well as increases thermal stability [18, 20]. It is also reported that the addition of Nb in Ni–Zr amorphous alloy systems had beneficial effects such as increasing crystallization temperature (T_x), fracture strength, hardness [16] and reduced susceptibility to hydrogen embrittlement. Furthermore, the Ni-based metallic glasses have desirable corrosion resistance in natural freshwater and alkaline media like sodium and potassium hydroxide due to passive film formation [25]. However, it is generally susceptible to pitting corrosion in chloride environments. It is reported that the Cl^- ion, because of its smaller diameter, is more aggressive than other halide ions which are readily adsorbed on weak areas of the passive film, resulting in the initiation of pitting [26] which is the most hazardous form of corrosion [27].

In this research, to make the Ni-Nb, Ni-Zr, and Ni-Nb-Zr alloy systems functional for a broader range of applications, a comprehensive investigation of thermal stability, corrosion resistance, and nano-indentation behavior of three $Ni_{60}Nb_{40}$, $Ni_{60}Nb_{20}Zr_{20}$, and $Ni_{60}Zr_{40}$ amorphous ribbons were assessed. While, in the previous researches the corrosion environment of Ni-based amorphous alloys was selected H_2SO_4 and HCl, in this study, the corrosion media was selected NaCl Solution to analyze the effect of Cl^- ion on corrosion resistance of these alloys for application of them in seawater and the importance of being safe in this environment.

2. Materials and methods

Pieces of elemental Ni (99.99% purity), Nb (99.8% purity), and Zr (99.7% purity) rods, from Johnson Matthey, were used as raw materials. Alloy

ingots with the nominal compositions of $Ni_{60}Nb_{40}$, $Ni_{60}Zr_{40}$, and $Ni_{60}Nb_{20}Zr_{20}$ (at. %) were prepared by arc melting method. Melt spinning was performed on a Cu wheel rotating with a tangential speed of 50 m/s in an inert Ar atmosphere. Melt spinning of $Ni_{60}Zr_{40}$, $Ni_{60}Nb_{20}Zr_{20}$, and $Ni_{60}Nb_{40}$ alloys resulted in continuous ribbons with typical dimensions of 20-30 μm in thickness and 1-1.5 mm in width. The compositions of the samples were determined using a Cameca Su30 electron microprobe analyzer with a wavelength-dispersive X-ray spectrometer (WDX). The results are shown in Table 1. The presence of Si element in compositions is due to the cleaning of ingots via SiC grinding paper followed by ultrasonic cleaning in methanol.

Melt-spun ribbons were characterized by X-ray diffractometer (Philips XPERT-MPD) with Cu Kα radiation (λ=0.1542 nm), time per step of 0.05 s at 2θ = 20-100º, and differential scanning calorimetry (DSC) in a TA2200 thermal analyzer fitted with a 2010 DSC module using a constant heating rate of 10 °C/min from 150–670 °C under a dynamic Ar atmosphere. The corrosion characteristics of $Ni_{60}Zr_{40}$, $Ni_{60}Nb_{20}Zr_{20}$, and $Ni_{60}Nb_{40}$ amorphous ribbons were evaluated by potentiodynamic polarization and electrochemical impedance spectroscopy (EIS) tests using an

Table 1- The chemical compositions of alloys (at. %)

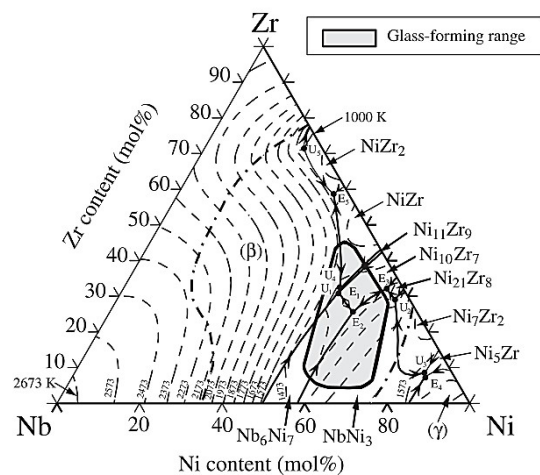| Sample	Ni	Nb	Zr	Si
$Ni_{60}Zr_{40}$	60.67	---	39.21	0.12
$Ni_{60}Nb_{20}Zr_{20}$	60.24	20.39	19.17	0.20
$Ni_{60}Nb_{40}$	60.10	39.85	---	0.05

Fig. 1- The calculated liquidus surface projection of the Nb-Ni-Zr system, together with the observed glass-forming compositional range (shaded area) and boundaries for amorphous-forming (dash-dotted lines) [16].

Ivium potentiostate/galvanostat. Potentiodynamic polarization experiments were performed at a potential scan rate of 1 mV/s in a potential range from -250 mV from OCP potential to 1.0 V. EIS measurements were performed at the open circuit potential (OCP) over a frequency range of 100 kHz to 10 mHz. The obtained EIS data were analyzed by curve fitting and electrical circuit modeling using Zview software. All the tests were performed in a three-electrode cell arrangement with a platinum plate as the counter electrode, Ag/AgCl electrode as the reference electrode and samples (0.6 cm² in area) as the working electrodes. The schematic of the used cell is shown in Fig. 2. The test solution consisted of 1 M NaCl, according to ref. [28] and all the samples were immersed in this solution for 20 min before each test.

The hardness and elastic modulus of samples were measured by the nano-indentation test. Prior to indentation, the samples were polished to a mirror-like appearance using a diamond paste, down to 1 μm-diamond particles. 15 measurements were done on each sample and the average of d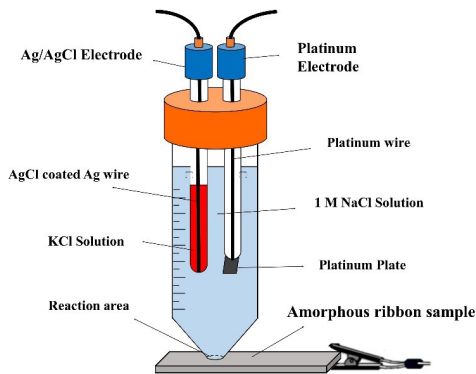ata was reported. The nano-indentation tests were performed using a nano-indentation tester (CSM instrument) with a Berkovich indenter tip and the maximum load of 20 mN. Olivier and Pharr's method [29] was used to determine the elastic modulus and hardness of samples. The equation (1) was used to calculate the elastic modulus [29].

$$\frac{1}{E_r} = \frac{\left(1 - v_i^2\right)}{E_i} + \frac{\left(1 - v_s^2\right)}{E_s} \tag{1}$$

Where, v and E is the poison ratio and elastic modulus, respectively. i and s stand for indenter and sample. E_i and v_i were 1141 GPa and 0.07 for a Berkovich indenter. The poison ratio of sample (v_s) was determined to be about 0.3 [29].

The Vickers hardness (H_V) was calculated using the equation (2), where F_m and A_d are the maximum force in the nano-indentation test and the developed area under indentor, respectively [29].

$$H_V = \frac{F_m}{A_d} \tag{2}$$

3. Results and discussion

3.1. Structural and thermal analysis of amorphous ribbons

XRD patterns of $Ni_{60}Zr_{40}$, $Ni_{60}Nb_{20}Zr_{20}$, and $Ni_{60}Nb_{40}$ melt-spun ribbons are presented in Fig. 3. Only a broad halo is observed on XRD patterns for all three alloys suggesting a fully amorphous structure.

The differential scanning calorimetry (DSC) was performed to reveal the crystallization behavior of the amorphous structure. Fig. 4 shows DSC traces of melt-spun ribbons of $Ni_{60}Zr_{40}$, $Ni_{60}Nb_{20}Zr_{20}$, and $Ni_{60}Nb_{40}$ alloys at a heating rate of 10 °C/min. There is one exothermic crystallization peak for $Ni_{60}Nb_{40}$ alloy while the DSC traces of $Ni_{60}Zr_{40}$ and $Ni_{60}Nb_{20}Zr_{20}$ alloys show two exothermic peaks from the two stages of crystallization.

Fig. 2- The schematic of a three-electrode cell arrangement.
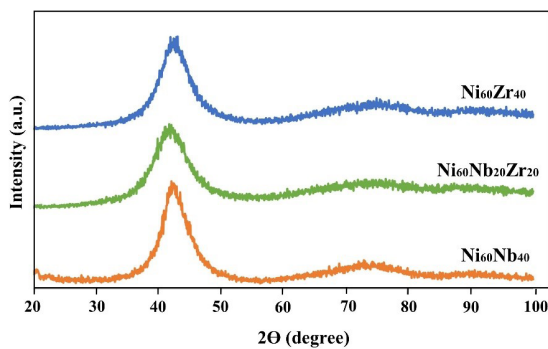
Fig. 3- XRD patterns of as-melt-spun ribbons of $Ni_{60}Zr_{40}$, $Ni_{60}Nb_{20}Zr_{20}$ and $Ni_{60}Nb_{40}$ alloys.
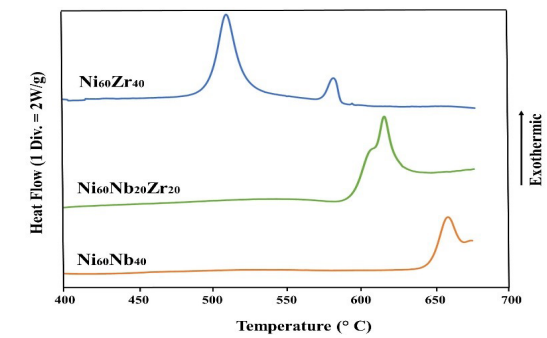
Fig. 4- DSC traces of as-melt-spun ribbons of $Ni_{60}Zr_{40}$, $Ni_{60}Nb_{20}Zr_{20}$ and $Ni_{60}Nb_{40}$ alloys.

The onset temperature (T_o) and peak temperature (T_P) of $Ni_{60}Zr_{40}$, $Ni_{60}Nb_{20}Zr_{20}$, and $Ni_{60}Nb_{40}$ alloys are presented in Table 2. The onset temperature (T_o) can be taken as a criterion to compare the relative thermal stability of the amorphous alloys [6]. As can be seen (Fig. 4), the onset temperature for crystallization of $Ni_{60}Nb_{40}$, $Ni_{60}Nb_{20}Zr_{20}$ and $Ni_{60}Zr_{40}$ alloys are 632, 593, and 476 °C, respectively. DSC results have shown that substitution of Nb with Zr reduces the thermal stability. As can be seen in Fig. 4, the T_o in $Ni_{60}Nb_{20}Zr_{20}$ alloy reduced for 39 °C while 156 °C reduction in T_o was observed in case of $Ni_{60}Zr_{40}$ alloy in comparison with $Ni_{60}Nb_{40}$. The crystallization temperature of amorphous structure is depended on the atomic radius, melting point and the bond valence of alloying components [30]. The higher melting point, higher bond valence and small atomic radius of Nb in comparison with Zr inhibit the formation of the low temperature intermediate crystalline phase and increase T_o in $Ni_{60}Nb_{40}$ alloy.

The crystallization product(s) of $Ni_{60}Zr_{40}$, $Ni_{60}Nb_{20}Zr_{20}$, and $Ni_{60}Nb_{40}$ alloys are listed in Table 2. More observation about XRD and DSC analysis is explained in a previous study from the authors [31-33]. Based on estimated time-temperature-transformation (TTT) curves for crystallization of Ni_3Nb, Ni_6Nb_7 and $Ni_{10}Zr_7$, Tokunaga et al. [19]

calculated that Ni_3Nb intermetallic compound forms during the crystallization of $Ni_{60}Nb_{20}Zr_{20}$ amorphous alloy which accord well with the results obtained in this work. The crystallization product of $Ni_{60}Zr_{40}$ amorphous alloy during crystallization was $Ni_{10}Zr_7$ intermetallic compound [6]. Formation of $Ni_{10}Zr_7$ intermetallic compound during crystallization of $Ni_{60}Zr_{40}$ amorphous alloy reported in other researches [34, 35]. The $Ni_{60}Nb_{40}$ amorphous alloy forms Ni_3Nb and Ni_6Nb_7 intermetallic compounds during crystallization. These results are in agreement with Gibbs free energy-composition diagram of Ni-Nb alloy that shows the lowest Gibbs free energy is achieved when Ni_3Nb and Ni_6Nb_7 crystalline compounds produces. The formation of two Ni_3Nb and Ni_6Nb_7 phases implies that the crystallization of $Ni_{60}Nb_{40}$ alloy occurs with an eutectic mechanism [31].

3.2. Corrosion behavior of amorphous ribbons

The potentiodynamic polarization curves of $Ni_{60}Nb_{40}$, $Ni_{60}Nb_{20}Zr_{20}$, and $Ni_{60}Zr_{40}$ amorphous alloys are presented in Fig. 5. As shown in Fig. 5, there is an increase in current density of anodic branches of all three alloys, due to the dissolution of metal ions from the alloy surface in 1 M NaCl solution, but with increasing potential, this active dissolution region was followed by a constant
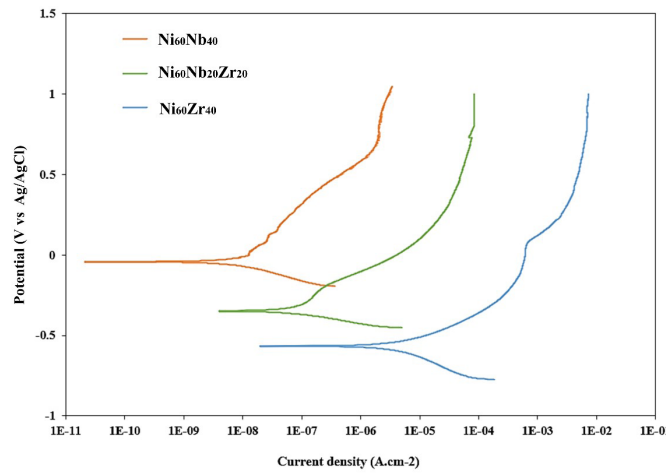
Fig. 5- Potentiodynamic polarization curves of $Ni_{60}Nb_{40}$, $Ni_{60}Nb_{20}Zr_{20}$ and $Ni_{60}Zr_{40}$ amorphous alloys after 20min immersion in 1 M NaCl solution.

Table 2- T_o, T_{P1}, T_{P2}, and crystallization products of $Ni_{60}Zr_{40}$, $Ni_{60}Nb_{20}Zr_{20}$ and $Ni_{60}Nb_{40}$ amorphous alloys.

Samples	T_o (°C)	T_{P1} (°C)	T_{P2} (°C)	Crystallization products
$Ni_{60}Nb_{40}$	632	658	---	Ni_3Nb, Ni_6Nb_7 [31]
$Ni_{60}Zr_{40}$	476	509	581	$Ni_{10}Zr_7$ [6]
$Ni_{60}Nb_{20}Zr_{20}$	593	---	623	Ni_3Nb [19]

current density region called passive range, due to the formation of a thin oxide/hydroxide film on the alloy surface. The existence of this active/passive behavior could be due to the simultaneous Ni dissolution, and continuous formation of Nb and Zr oxide film, which reported similarly in ref. [36]. This passive film can cover the surface of alloys and protects them from the further dissolution of metal ions. This in turn prevents aggressive ion penetration and more corrosion reflecting better corrosion resistance [37]. The corrosion potential (E_{corr}) and passive current density (i_{pass}) were estimated from the polarization curves and reported in Table 3.

As known, the higher E_{corr} and the lower i_{pass} show nobler and better corrosion behavior therefore, according to Table 3, the highest E_{corr} and the lowest i_{pass} are obtained for $Ni_{60}Nb_{40}$ alloy. This appropriate corrosion behavior can be attributed

to the formation of a Nb-rich oxide film on the surface of the alloy [38, 39].

Fig. 6 shows SEM images of surface morphologies of corroded ribbons in the presence of chloride solution after polarization test along with energy-dispersive X-ray spectroscopy (EDS) analysis.

Fig. 6a, shows the corroded $Ni_{60}Zr_{40}$ ribbon, which accompanied by breakdowns and development of pits. As illustrated in the $Ni_{60}Zr_{40}$ polarization plot (Fig. 5), breakdown occurs in 0.062 V in the presence of chloride solution. Furthermore, $Ni_{60}Zr_{40}$ is heavily attacked by chloride ions and half droplet-shaped features appeared on its surface, as illustrated in polarization plots. Previous studies reported that Ni-Zr amorphous alloys are completely susceptible to pitting in chloride environments [40, 41]. However, as can be observed in the Fig. 6, although $Ni_{60}Nb_{20}Zr_{20}$ alloy (Fig. 6b) appears to be severely

Table 3- Electrochemical parameters extracted from Figure 5

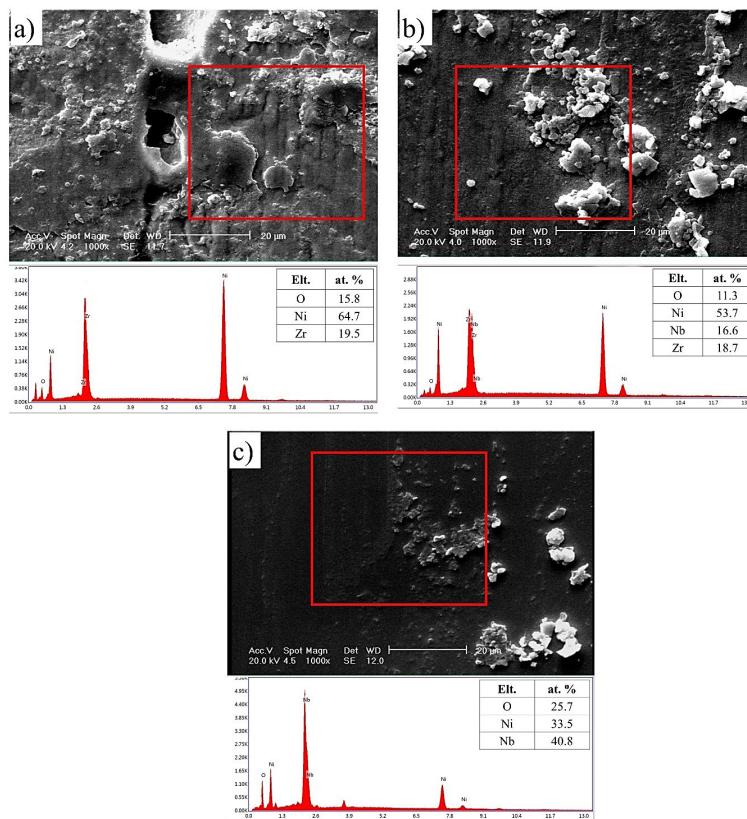| Samples	E_{corr} (V vs Ag/AgCl)	i_{pass} (μA.cm^{-2})
$Ni_{60}Nb_{40}$	-0.052	1.4
$Ni_{60}Nb_{20}Zr_{20}$	-0.356	15
$Ni_{60}Zr_{40}$	-0.572	360

Fig. 6- Surface morphologies and EDS of the corroded surfaces of alloys: a) $Ni_{60}Zr_{40}$, b) $Ni_{60}Nb_{20}Zr_{20}$, and c) $Ni_{60}Nb_{40}$.

damaged and corrosion products are observed on the ribbon surface, pitting corrosion does not occur in $Ni_{60}Nb_{20}Zr_{20}$ amorphous alloy due to the higher stability of the passive films, which stems from the presence of Nb [42]. Furthermore, surface examination of corroded $Ni_{60}Nb_{40}$ ribbons after polarization test (Fig. 6c) revealed that $Ni_{60}Nb_{40}$ shows a smooth morphology without any significant attack attributed to the protective nature of the passive film.

According to EDS analysis, the concentration of Ni is more on the surface of corroded $Ni_{60}Zr_{40}$ and $Ni_{60}Nb_{20}Zr_{20}$ ribbons rather than $Ni_{60}Nb_{40}$ ribbon, which indicate a lack of uniform passive film on the surfaces. The higher Nb content in comparison to Ni content in $Ni_{60}Nb_{40}$ EDS analysis shows not only the lower diffusion of Ni in the surface but also illustrates the positive role of Nb as a protective element against corrosion damages [43]. Moreover, the lower amount of Ni and high level of oxygen in the corroded surface area in Ni60Nb40 alloy resulted from the formation of the stable passive film due to the presence of Nb. Therefore, based on potentiodynamic polarization test (Fig. 5) and SEM images (Fig. 6), corrosion performance in all alloys are in the following order: $Ni_{60}Nb_{40}$ > $Ni_{60}Nb_{20}Zr_{20}$ > $Ni_{60}Zr_{40}$.

For further examination, EIS tests were performed on the $Ni_{60}Nb_{40}$, $Ni_{60}Nb_{20}Zr_{20}$, and $Ni_{60}Zr_{40}$ amorphous alloys. The EIS results are illustrated in Fig. 7. It is generally accepted that amorphous alloys are uniform and free from any crystalline defects such as segregations, dislocations, grain boundaries, precipitates, stacking faults [37]. This nature of amorphous alloys is believed as one of the reasons for their high corrosion resistance as shown in Fig. 7. All the Nyquist and Bode modulus plots exhibited one-time constant. Therefore, the one-time constant equivalent electrical circuit which is reported in recent researches [44, 45] is used for fitting the impedance spectra of ribbon samples (Fig. 6). R_s, R_p, and CPE indicate the solution resistance, polarization resistance, and constant phase element, respectively. The impedance of CPE is given by equation [46]:

$$Z_{CPE} = Y_0 (j\omega)^{-n} \tag{3}$$

Where Y_0 is a constant ($\Omega^{-1}S^n$), n is the power index value of CPE, ω is the angular frequency, and j is the imaginary number equal to $\sqrt{-1}$. The conversion of Y_0 to the capacitance value is described using the following equation:

$$C = Y_0 (\omega_m'')^{n-1} \tag{4}$$

Where C is the capacitance of the passive film and ω_m'' is the frequency at which the imaginary part of the impedance Z″ has a maximum. The CPE is used for obtaining a better fit of the experimental impedance plots and for all the conditions, the power index values are in the range of 0.85–0.9 which suggested that the deviation from pure
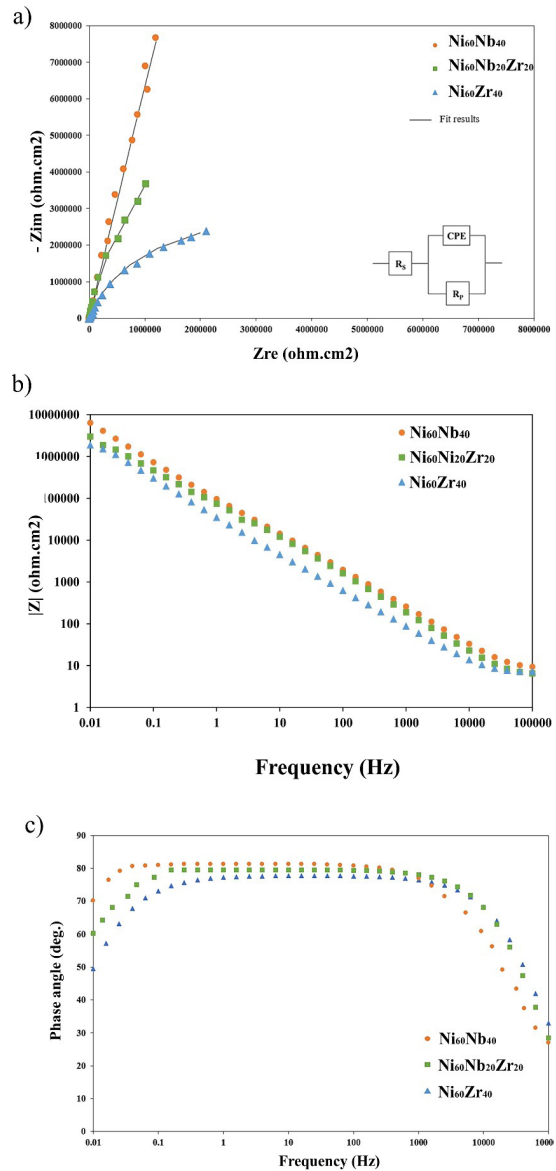
Fig. 7- a) Nyquist plots and b) Bode plots and c) bode phase plots of amorphous ribbons after 20 min immersion in 1 M NaCl solution.

capacitance is relatively small. Obtained data are summarized in Table 4. According to Table 4, the higher polarization resistance and the lower capacitance value of $Ni_{60}Nb_{40}$ compared to other ribbon samples could be correlated to the high stability of the passive film formed on $Ni_{60}Nb_{40}$. The stability of the passive film is attributed to the low diffusion of ionic species and/or low charge transfer and their accumulation across the film/solution interface. It is noticeable that EIS and polarization results show a similar trend.

3.3. Nano-indentation behavior of amorphous ribbons

Fig. 8 shows the load (P)–displacement (h) curves for $Ni_{60}Zr_{40}$, $Ni_{60}Nb_{20}Zr_{20}$, and $Ni_{60}Nb_{40}$ amorphous ribbons.

The results of hardness and Young modulus for $Ni_{60}Zr_{40}$, $Ni_{60}Nb_{20}Zr_{20}$ and, $Ni_{60}Nb_{40}$ amorphous alloys presented in Table 5 along with the results reported in the literature. As can be seen (Fig. 8), the maximum penetration depth at the end of the load holding segment is higher for $Ni_{60}Nb_{20}Zr_{20}$ alloy in comparison with $Ni_{60}Zr_{40}$ and $Ni_{60}Nb_{40}$ amorphous alloys. It means that $Ni_{60}Nb_{20}Zr_{20}$ amorphous alloy is mechanically softer. In fact, the hardness values for the ribbons are very high (about 12-15GPa). The maximum hardness (15.01 ± 0.69) and minimum hardness (12.16 ± 0.75) were for $Ni_{60}Nb_{40}$ and $Ni_{60}Nb_{20}Zr_{20}$ amorphous alloys, respectively. The slope of the unloading segments is slightly slower for $Ni_{60}Nb_{20}Zr_{20}$ alloy in comparison with $Ni_{60}Zr_{40}$ and $Ni_{60}Nb_{40}$ amorphous alloys, indicating that the stiffness value of the $Ni_{60}Nb_{20}Zr_{20}$ alloy is lower. The calculated elastic modulus using nano-indentation test are listed in Table 5 confirm that the elastic

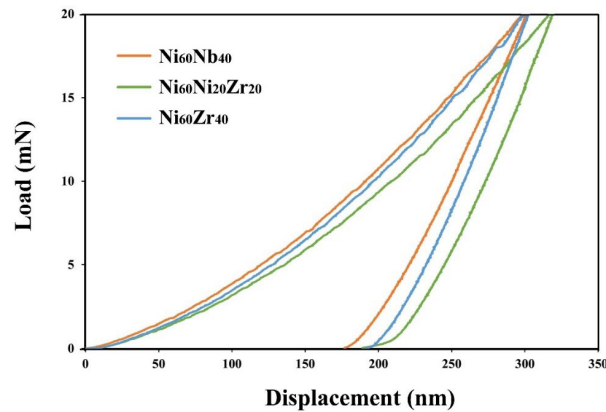Fig. 8- Load–displacement (P–h) curves for $Ni_{60}Zr_{40}$, $Ni_{60}Nb_{20}Zr_{20}$ and $Ni_{60}Nb_{40}$ amorphous ribbons.

Table 4- EIS elements values from equivalent electrical circuit

Amorphous ribbons	R_s ($\Omega.cm^2$)	R_P ($M\Omega.cm^2$)	CPE_{MG} ($\mu F.cm^{-2}.s^{n-1}$)	n_0	$\chi 2$
$Ni_{60}Nb_{40}$	6.91	936	1.77	0.88	0.018
$Ni_{60}Nb_{20}Zr_{20}$	6.57	49	2.21	0.90	0.036
$Ni_{60}Zr_{40}$	4.56	16	2.77	0.86	0.043

Table 5- Mechanical properties of some related Ni-based alloy systems

Alloy system	Methods	Mechanical properties			Ref.
		Young's modulus (GPa)	Hardness (GPa)	Hardness (H_v)*	
$Ni_{60}Nb_{40}$	Nano-indentation	171.3 ± 8.14	15.01 ± 0.69	1531±70.36	Present Study
$Ni_{60}Nb_{20}Zr_{20}$	Nano-indentation	160.41 ± 8.19	12.16 ± 0.75	1240±76.47	Present Study
$Ni_{60}Zr_{40}$	Nano-indentation	188.52 ± 7.33	14.13 ± 0.84	1441±85.65	Present Study
$Ni_{59.5}Nb_{40.5}$	Nano-indentation	190 ± 8	11.5 ± 0.30	1173 ± 30.6	[5]
$Ni_{61.5}Nb_{38.5}$	Compression	170	---	---	[20]
$Ni_{61.5}Nb_{33.5}Zr_5$	Compression	130	---	---	[20]
$Ni_{62}Nb_{32.3}Zr_{5.7}$	Compression	128	---	---	[20]
$Ni_{63}Nb_{31.45}Zr_{5.55}$	Compression	127	---	---	[20]
$Ni_{50}Nb_{28}Zr_{22}$	Nano-indentation	89 ± 3	9.5 ± 0.30	968.7 ± 30.6	[17]

Table 6- Summary of obtained results from thermal analysis, corrosion resistance and mechanical properties for $Ni_{60}Zr_{40}$, $Ni_{60}Nb_{20}Zr_{20}$ and $Ni_{60}Nb_{40}$ amorphous ribbons

Alloy system	Thermal analysis			polarization resistance	Mechanical properties	
	T_o (°C)	T_{P1} (°C)	T_{P2} (°C)	Rct ($M\Omega.cm^2$)	Young's modulus (GPa)	Hardness (Hv)
$Ni_{60}Nb_{40}$	632	658	---	936	171.30 ± 8.14	1531±70.36
$Ni_{60}Nb_{20}Zr_{20}$	593	---	623	49	160.41 ± 8.19	1240±76.47
$Ni_{60}Zr_{40}$	476	509	581	16	188.52 ± 7.33	1441±85.65

modulus of the $Ni_{60}Nb_{20}Zr_{20}$ amorphous alloy is the minimum value (160.41 ± 8.19 GPa).

It is asserted that one of the important mechanisms of plastic deformation in amorphous metallic materials is shear band mechanism. In this mechanism, due to the random arrangement of atoms in amorphous state, some zones have higher density compared to the whole material. By applying an external loading, atoms in these dense areas can move on each other more easily rather than other areas, thus a very tiny area (small bands) can be created. Since these small bands carry inhomogeneous plastic deformation, they are called shear band mechanism [1]. During nanoindentation test in amorphous materials, pop-in events or serrations in P-h curve are related to this phenomenon. The clear serrations in the loading segment of curves (Fig. 8) of each $Ni_{60}Zr_{40}$, $Ni_{60}Nb_{20}Zr_{20}$ and, $Ni_{60}Nb_{40}$ amorphous ribbons are related to the formation and propagation shear bands [5, 47, 48].

Table 6 lists a summary of obtained results from the thermal analysis, corrosion resistance, and mechanical properties of $Ni_{60}Zr_{40}$, $Ni_{60}Nb_{20}Zr_{20}$, and $Ni_{60}Nb_{40}$ amorphous ribbons. As can be seen, the complete substitution of Zr with Nb in the amorphous structure improved the thermal stability, corrosion resistance, and hardness of amorphous alloy.

4. Conclusion

Microstructure, crystallization mechanism, corrosion, and nanoindentation behaviour of the Ni60Zr40, Ni60Zr20Nb20, and Ni60Nb40 amorphous alloys were investigated. The comparison of the thermal stabilities of Ni60Zr40, Ni60Zr20Nb20, and Ni60Nb40 amorphous alloys by the DSC shows that the presence of Nb improved the thermal stability of amorphous alloys against crystallization. The maximum thermal stability (632 °C) was found for Ni60Nb40 amorphous alloy. The uniform nature of amorphous structure and presence of the noble and passive element of Nb and Zr in these amorphous structures shows an appropriate corrosion resistance in NaCl solution. For example, the potentiodynamic polarization results showed the polarization resistance value of 936, 49, and 16 MΩ.cm2 for Ni60Nb40, Ni60Nb20Zr20, and Ni60Zr40 amorphous alloys, respectively. Nano-indentation results indicated that the presence of Nb increased the hardness of amorphous structure to 15.01 ± 0.69 GPa for Ni60Nb40 amorphous alloy.

References

1. C. Suryanarayana and A. Inoue, *Bulk Metallic Glasses*. CRC Press, 2017.
2. Dastanpour E, Masood A, Enayati MH, Ström V. Multi-alloying of nanomet: conception and implementation of homogeneous nanocrystallization in high-flux density soft magnetic alloys. Journal of Materials Science. 2021;56(16):10124-34.
3. Imani M, Enayati MH, Basak AK. A novel approach for mechanical alloying amorphisation in magnetic Fe–Co alloy system. Materials Research Express. 2019;6(7):076575.
4. Halim Q, Mohamed NAN, Rejab MRM, Naim WNWA, Ma Q. Metallic glass properties, processing method and development perspective: a review. The International Journal of Advanced Manufacturing Technology. 2021;112(5-6):1231-58.
5. Concustell A, Mattern N, Wendrock H, Kuehn U, Gebert A, Eckert J, et al. Mechanical properties of a two-phase amorphous Ni–Nb–Y alloy studied by nanoindentation. Scripta Materialia. 2007;56(2):85-8.
6. Enayati MH, Schumacher P, Cantor B. Journal of Materials Science. 2002;37(24):5255-9.
7. Xia L, Li WH, Fang SS, Wei BC, Dong YD. Binary Ni–Nb bulk metallic glasses. Journal of Applied Physics. 2006;99(2):026103.
8. Hara S, Sakaki K, Itoh N, Kimura HM, Asami K, Inoue A. An amorphous alloy membrane without noble metals for gaseous hydrogen separation. Journal of Membrane Science. 2000;164(1-2):289-94.
9. Donten M, Cesiulis H, Stojek Z. Electrodeposition of amorphous/nanocrystalline and polycrystalline Ni–Mo alloys from pyrophosphate baths. Electrochimica Acta. 2005;50(6):1405-12.
10. Hara S, Hatakeyama N, Itoh N, Kimura HM, Inoue A. Hydrogen permeation through palladium-coated amorphous Zr☐M☐Ni (M = Ti, Hf) alloy membranes. Desalination. 2002;144(1-3):115-20.
11. Imani M, Dastanpoor E, Enayati MH, Basak AK. Thermodynamic Prediction of Phase Formation in Ni–P Alloy System During Mechanical Alloying: Comparison with Electroless Plating Technique. Metals and Materials International. 2020;27(6):1366-73.
12. Wang D, Kong L-B, Liu M-C, Zhang W-B, Luo Y-C, Kang L. Amorphous Ni–P materials for high performance pseudocapacitors. Journal of Power Sources. 2015;274:1107-13.

13. Deo LP, Kaufman MJ, Wang B, Nikodemski S, De Oliveira MF. Crystalline phases found in rapidly quenched Ni-Nb-Zr alloys. Journal of Microscopy. 2017;267(1):49-56.

14. Enayati MH. *Mechanical alloying of Ni-base alloys* (Doctoral dissertation, University of Oxford).

15. Enayati MH, Dastanpoor E. Two-stage amorphization reaction in Ni–Nb–Zr system. Advanced Powder Technology. 2015;26(5):1364-70.

16. Kimura H, Inoue A, Yamaura S-i, Sasamori K, Nishida M, Shinpo Y, et al. Thermal Stability and Mechanical Properties of Glassy and Amorphous Ni-Nb-Zr Alloys Produced by Rapid Solidification. MATERIALS TRANSACTIONS. 2003;44(6):1167-71.

17. Santos FS, Sort J, Fornell J, Baró MD, Suriñach S, Bolfarini C, et al. Mechanical behavior under nanoindentation of a new Ni-based glassy alloy produced by melt-spinning and copper mold casting. Journal of Non-Crystalline Solids. 2010;356(43):2251-7.

18. Sarker S, Chandra D, Hirscher M, Dolan M, Isheim D, Wermer J, et al. Developments in the Ni–Nb–Zr amorphous alloy membranes. Applied Physics A. 2016;122(3).

19. Tokunaga T, Matsumoto S, Ohtani H, Hasebe M. Thermodynamic Analysis of the Phase Equilibria in the Nb-Ni-Zr System. Journal of the Japan Institute of Metals. 2006;70(9):741-9.

20. Zhu ZW, Zhang HF, Ding BZ, Hu ZQ. Synthesis and properties of bulk metallic glasses in the ternary Ni–Nb–Zr alloy system. Materials Science and Engineering: A. 2008;492(1-2):221-9.

21. Paglieri SN, Pal NK, Dolan MD, Kim S-M, Chien W-M, Lamb J, et al. Hydrogen permeability, thermal stability and hydrogen embrittlement of Ni–Nb–Zr and Ni–Nb–Ta–Zr amorphous alloy membranes. Journal of Membrane Science. 2011;378(1-2):42-50.

22. Tokunaga T, Matsumoto S, Ohtani H, Hasebe M. Thermodynamic Analysis of the Phase Equilibria in the Nb-Ni-Zr System. MATERIALS TRANSACTIONS. 2007;48(9):2263-71.

23. Dolan M, Dave N, Morpeth L, Donelson R, Liang D, Kellam M, et al. Ni-based amorphous alloy membranes for hydrogen separation at 400°C. Journal of Membrane Science. 2009;326(2):549-55.

24. Takahashi T, Higashi Si, Kai T, Kimura H, Masumoto T. Benzene hydrogenation activity of nickel catalysts prepared from amorphous Ni-Zr alloys. Catalysis Letters. 1994;26(3-4):401-9.

25. Wang S, Xu D, Guo Y, Tang X, Wang Y, Zhang J, et al. Corrosion Behavior of Alloy Steels in Supercritical Water Environments. Supercritical Water Processing Technologies for Environment, Energy and Nanomaterial Applications: Springer Singapore; 2019. p. 149-259.

26. Soltis J. Passivity breakdown, pit initiation and propagation of pits in metallic materials – Review. Corrosion Science. 2015;90:5-22.

27. Bhandari J, Khan F, Abbassi R, Garaniya V, Ojeda R. Modelling of pitting corrosion in marine and offshore steel structures – A technical review. Journal of Loss Prevention in the Process Industries. 2015;37:39-62.

28. Tan CG, Jiang WJ, Zhang ZC, Wu XQ, Lin JG. The effect of Ti-addition on the corrosion behavior of the partially crystallized Ni-based bulk metallic glasses. Materials Chemistry and Physics. 2008;108(1):29-32.

29. Oliver WC, Pharr GM. An improved technique for determining hardness and elastic modulus using load and displacement sensing indentation experiments. Journal of Materials Research. 1992;7(6):1564-83.

30. Dolan MD, Hara S, Dave NC, Haraya K, Ishitsuka M, Ilyushechkin AY, et al. Thermal stability, glass-forming ability and hydrogen permeability of amorphous Ni64Zr36–XMX (M=Ti, Nb, Mo, Hf, Ta or W) membranes. Separation and Purification Technology. 2009;65(3):298-304.

31. Enayati MH. Crystallization behavior of Ni-Nb amorphous alloys.

32. Enayati MH. *Mechanical alloying of Ni-base alloys* (Doctoral dissertation, University of Oxford).

33. Enayati MH, Chang IT, Schumacher P, Cantor B. Mechanical alloying of Ni-Nb alloys. InMaterials Science Forum 1997 (Vol. 235, pp. 85-90). Trans Tech Publications Ltd.

34. Altounian Z, Guo-hua T, Strom-Olsen JO. Crystallization characteristics of Ni-Zr metallic glasses from Ni20Zr80 to Ni70Zr30. Journal of Applied Physics. 1983;54(6):3111-6.

35. Dong YD, Gregan G, Scott MG. Formation and stability of nickel-zirconium glasses. Journal of Non-Crystalline Solids. 1981;43(3):403-15.

36. Daniel AA, Vasantha VS, Eric F. Evaluation of corrosion behavior of an amorphous Ni60Nb40–alloy with its crystalline form in stimulated nitric PEMFC conditions. Journal of Dispersion Science and Technology. 2019;41(7):1022-9.

37. Hashimoto K, Kumagai N, Yoshioka H, Kim JH, Akiyama E, Habazaki H, et al. Corrosion-resistant amorphous surface alloys. Corrosion Science. 1993;35(1-4):363-70.

38. Liu S, Huang L, Pang S. Effect of microstructure on corrosion behaviours of a Ni-based metallic glass. Rare Metals. 2011;30(S1):529-32.

39. Poddar C, Ningshen S, Jayaraj J. Corrosion assessment of Ni60 Nb30Ta10 metallic glass and its partially crystallized alloy in concentrated nitric acid environment. Journal of Alloys and Compounds. 2020;813:152172.

40. Janik-Czachor M. Stability of the Passive State of Ni-Zr Glassy Alloys. CORROSION. 1993;49(9):763-8.

41. Kawashima A, Yu WP, Zhang BP, Habazaki H, Asami K, Hashimoto K. Pitting Corrosion of Amorphous Ni&ndash;Zr Alloys in Chloride Ion Containing Sulfuric Acid Solutions. Materials Transactions, JIM. 1997;38(5):443-50.

42. Jayalakshmi S, Vasantha VS, Fleury E, Gupta M. Characteristics of Ni–Nb-based metallic amorphous alloys for hydrogen-related energy applications. Applied Energy. 2012;90(1):94-9.

43. Jayaraj J, Nanda Gopala Krishna D, Mallika C, Kamachi Mudali U. Passive film properties and corrosion behavior of Ni–Nb and Ni–Nb–Ta amorphous ribbons in nitric acid and fluorinated nitric acid environments. Materials Chemistry and Physics. 2015;151:318-29.

44. Poddar C, Jayaraj J, Amirthapandian S, Ningshen S. Effect of thermally grown amorphous oxide film on the corrosion resistance properties of Ni50Zr25Nb25 metallic glass in nitric acid medium. Intermetallics. 2019;113:106571.

45. D. N. G. K. J. Jayaraj, C. Mallika, U. Kamachi Mudali, "Passive film properties and corrosion behavior of NieNb and NieNbeTa amorphous ribbons in nitric acid and fluorinated nitric acid Environments," *Materials Chemistry and Physics,* vol. 1, 2014.

46. Poddar C, Jayaraj J, Ningshen S, Mudali UK. Effect of thermal oxidation on the oxide characteristic and corrosion behavior of Ni60Nb40 amorphous ribbon in nitric acid. Applied Surface Science. 2019;479:430-9.

47. Schuh CA, Lund AC, Nieh TG. New regime of homogeneous flow in the deformation map of metallic glasses: elevated temperature nanoindentation experiments and mechanistic modeling. Acta Materialia. 2004;52(20):5879-91.

48. Medeiros BB, Medeiros MM, Fornell J, Sort J, Baró MD, Jorge AM. Nanoindentation response of Cu–Ti based metallic glasses: Comparison between as-cast, relaxed and devitrified states. Journal of Non-Crystalline Solids. 2015;425:103-9.